EUROPEAN ORGANIZATION FOR NUCLEAR RESEARCH
ORGANISATION EUROPÉENNE POUR LA RECHERCHE NUCLÉAIRE

CERN - TS Department

EDMS Nr: 679126 TS-Note-2005-055
Group reference: TS/LEA

Final papers from TS/LEA presented at

THE RADECS 2005 CONFERENCE ON "RADIATION AND ITS EFFECTS ON COMPONENTS AND SYSTEMS"

Held at Cap d'Agde, France, 19-23 September 2005

- GAMMA-RAY INDUCED OPTICAL ABSORPTION IN GE AND P-DOPED FIBRES AT THE LHC
- RADIATION TOLERANT COMMERCIAL OF THE SHELF COMPONENTS FOR THE REMOTE READOUT OF RADFETS AND PIN DIODES
- RADIATION INDUCED EFFECTS ON THE SENSORS OF THE HYDROSTATIC LEVELING SYSTEM FOR THE LHC LOW BETA QUADRUPOLES
- DOSIMETRY ASSESSMENTS IN THE IRRADIATION FACILITIES AT THE CERN-PS ACCELERATOR

Geneva, October 2005

GAMMA-RAY INDUCED OPTICAL ABSORPTION IN GE AND P-DOPED FIBRES AT THE LHC

Authors:

A. Presland, T. Wijnands & L. De Jonge , CERN Geneva, Switzerland.
T. Sugito, Draka Comteq NKF Kabel B.V., Gouda, Netherlands

Keywords: optical fibres, radiation induced attenuation, LHC

Geneva, October 2005

1. INTRODUCTION

Many LHC electronics will be installed in the tunnel close to beam in order to optimise performance, increase the S/N ration and to reduce cabling costs. The 3 major distributed control systems in the tunnel that use WorldFIP protocol over fibre optical links are the Quench Protection System, Power Converters and the Cryogenics system. Another big consumer of fibres in the tunnel is the BLM/BPM system that transmits raw data from the low level BPMs/BLMs crates directly over a fibre optical links to the surface at a rate of 40 MHz.

However, fibres in the LHC tunnel will suffer from radiation-induced attenuation, which may eventually halt the communication of data after a few years of nominal operation of the LHC. Radiation-induced attenuation depends mainly on the type and the concentration of dopants (such as Phosphor (P), Fluorine (F) and Germanium (Ge)) in the amorphous silicon dioxide (a-SiO_2) fibre core. At present Ge-P-doped and Ge-doped fibres are being installed in the LHC tunnel.

2. ATTENUATION OF LIGHT IN A FIBRE

The attenuation for a fibre is specified in decibels per kilometer (dB/km). When they are delivered at CERN, the single mode fibres used in the LHC tunnel have an attenuation of approximately 0.35 dB/km for light at 1310 nm. For a complete fibre connection between 2 points, the attenuation will be superior to this number because of the optical joints and connectors.

In addition to the decreasing attenuation with increasing wavelength, several spikes in the attenuation curve may be present if the SiO_2 contains impurities or structural or point defects. Even if the sample is initially free of absorption spikes, some may appear if the sample is exposed to radiation. This is because the radiation can activate pre-existing point defects that then begin to absorb photons of a specific energy. It can also create totally new point defects. The wavelength at which the defects absorb will depend on the structure of the point defect and, if it involves a dopant atom, the type of dopant involved.

Concurrent with the damage process, thermal and optical bleaching processes occur. These cause deactivation of absorption centres, for example by the liberation of a trapped charge. Activation and deactivation of absorption centres reaches equilibrium at a value of attenuation that depends on the dose rate. Attenuation will then be observed to saturate. Once irradiation has terminated activation will cease but the recovery processes will continue. This leads to the observation of short term recovery of fibre transmission. The radiation induced absorption centres continue to exist and once irradiation is resumed the attenuation levels quickly return to the saturating value as new charge carriers are created by radiolysis and start to populate the traps.

3. KINETIC MODELLING OF RADIATION INDUCED ATTENUATION

The dependence of the saturation value on dose rate (and temperature) is easily seen in a simple, first order kinetic formulations for defect generation. Considering the equation [2]

$$\frac{\partial n}{\partial t} = a\dot{D} - \frac{n}{\tau} \qquad (3.1)$$

where n is the defect concentration, $\dot{D}$ the dose-rate, a the probability of defect generation and τ the characteristic lifetime of the defect. For an isothermal, constant dose-rate regime, the solution of (3.1) is a saturating exponential of the form:

$$n = a\dot{D}\tau\left(1 - \exp\left(-t/\tau\right)\right) \qquad (3.2)$$

Since the characteristic lifetime of the defect, τ, is temperature dependent, it may be clear that the overall attenuation of light in a doped fibre is dose rate and temperature dependent.

To describe the experimental data presented in the next section we have used the kinetic model of Kyoto et al [3]. This model considers the sum of saturating exponentials to describe the overall attenuation of light *A(t)*:

$$A(t) = \sum_{i=1}^{n-1}\left[K_i\left(1 - \exp\left(-t/\tau_i\right)\right)\right] \qquad (3.3)$$

The constants $K_{1,2\ldots n-1}$ correspond to the saturation values of the different contributions to the induced attenuation and are dependent on the dose rate However, most of the radiolysis attenuation as described by (3.4), will anneal when irradiation is stopped. For the period after irradiation, the recovery of the induced radiation is parameterised:

$$A(t) = \sum_{j=1}^{m-1}\left[A_j \exp\left(-t/\tau_j\right)\right] \qquad (3.4)$$

After the annealing period the attenuation in the fibres do not, however, regain the initial values before irradiation. In the absence of transient effects related to the dose rate, it is reasonable to assume that the number of colour defect centres (and thus the optical absorption of the fibre) is proportional to the total absorbed dose.

$$A(t) = K_n(D) \qquad (3.5)$$

The range over which expression (3.5) is valid is limited because of the known saturation at very high doses and the transients observed during intense, pulsed irradiation. However, after a sufficiently long shutdown period, the attenuation in a LHC fibre in the tunnel will be almost entirely determined by the value of the total accumulated dose.

4. EXPERIMENTAL SETUP

The attenuation of the LHC type fibres under irradiation was studied in detail by irradiating the 2 types of LHC fibre with gamma rays from ^{60}Co in the POSEIDON irradiator at the nuclear

centre of CEA-Saclay in Paris. The aim of the experiment was two-fold: (1) confirm the radiation induced attenuation as predicted by literature and earlier experiments in the TCC2 test area and (2) verify the resistance of the mini-tubes after irradiation to ensure that fibres can still be replaced even after several years of LHC operation.

At the time of the experiment, the intensity of the ^{60}Co source was 631 kCi (22.5 kW). The dose rate at which the samples are exposed can be varied by increasing or decreasing the distance to the source. We choose to expose the cable drums at dose rates of 500 and 1000 Gy per hour. Each cable drum contained 1 km of SM fibre in a polyethylene minitube. The first cable drum was wound with the Ge-P doped MCVD produced SM fibre from Draka NK Cables Ltd and exposed at a dose rate of 500 Gy/hr. The second drum contained 1 km of Ge-doped PCVD SM fibre from Draka Fibre Technology BV and was exposed at 1000 Gy/hr.

Attenuation during irradiation was measured with an Optical Time Domain Reflectometer (OTDR). The OTDR injects a series of optical pulses into the fibre and measured the intensity of light that is scattered and reflected back. By the integrated intensity of the return pulses as a function of time, one can estimate the fibre's length and overall attenuation.

5. ATTENUATION UNDER IRRADIATION

5.1 Ge-Doped SM fibres

Figures 1 (a) and 1 (b) show the radiation-induced attenuation in the Ge-doped LHC SM fibre sample when irradiated at 1 kGy/hr. The irradiation was interrupted after approximately 33 minutes for approximately 2.5 hrs to study the annealing behaviour. Figure 1 (a) shows the attenuation data as function of time. This figure clearly shows the strong annealing effect when irradiation is interrupted. The attenuation in the fibres does not, however, regain the initial values before irradiation. When the samples are irradiated again, the attenuation follows the same saturating exponential development as before. After the second annealing period the remnant attenuation is higher (indicated with arrows) than after the first annealing period suggesting the existence of a dose dependent, linear contribution as in (3.5).

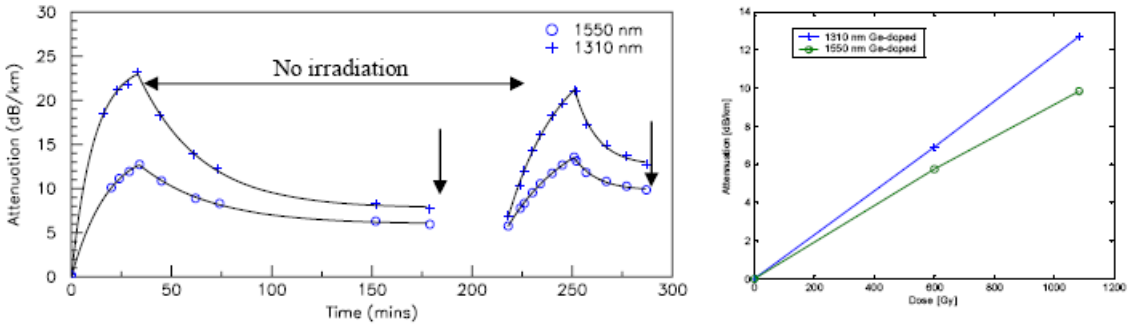

Figure 1 (a) Radiation induced attenuation of an LHC fibre (Ge-doped SM fibre) as a function of time (dose rate 1000 Gy/hour). The kinetic model fits to the growth and anneal data have been superimposed. Figure 1(b) Radiation induced attenuation in Ge doped SM fibres as a function of the total accumulated dose after complete annealing at room temperature (data points indicated with an arrow).

The existence of a linear term has been investigated further in figure 1 (b), which shows the attenuation of the Ge doped SM fibre as a function of total dose after each annealing period (i.e. the points indicated with arrows in figure 1(a)). The dependence on dose is quasi linear and approximately equal to 0.01 dB/km per Gy for light at either wavelength.

5.2 Ge-P-Doped SM fibres

Figure 2 shows the radiation-induced attenuation of the Ge-P-doped SM fibres as a function of the time for the same two wavelengths. The Ge-P-doped SM fibre in this experiment was irradiated at 500 Gy/hr. In contrast with the Ge-doped SM fibres, the Ge-P-doped SM fibre does not show any short term annealing and the attenuation is approximately equal to 0.08 dB/km per Gy for 1310 nm and 0.12 dB/km per Gy for light at 1550 nm.

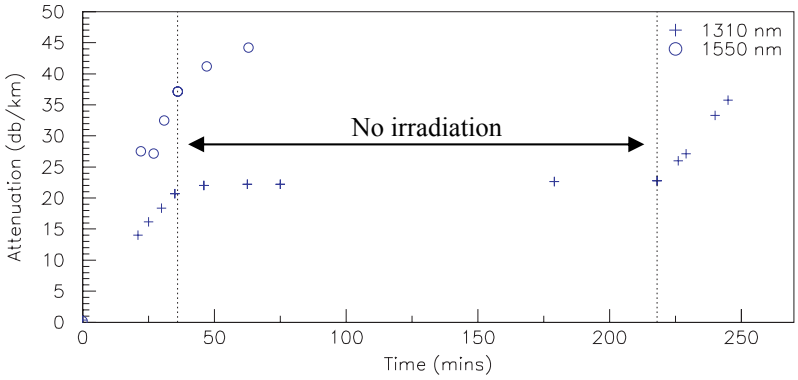

Figure 2. Radiation induced attenuation of the Ge-P-doped SM fibre as a function of time (dose rate 500 Gy/hour).

6. FIT TO KINETIC MODELS

The formulations derived in section 3 have been used to fit the attenuation data for the Ge-doped fibre during irradiation and annealing. The resulting plots are shown in figure 1a with the fit parameters tabulated below.

Damage fit coefficients	**1310 nm Ge-doped fibre**	**1550 nm Ge-doped fibre**
K_1 [dB/km]	24.20	14.50
τ_1[mins]	11.16	17.40

Table I. Fitting parameters for the radiation-induced attenuation in Ge doped SM fibres for light at 1310 nm and 1550 nm.

Recovery fit coefficients	**1310 nm Ge-doped fibre**	**1550 nm Ge-doped fibre**
A_1 [dB/Gy.km]	15.34	6.75
τ_1[mins]	31.14	35.92

Table II. Fitting parameters for the annealing at room temperature of the radiation-induced attenuation in Ge doped SM fibres for light at 1310 nm and 1550 nm.

The dynamic response of Ge-doped SM fibres under irradiation at 1 kGy/hr can be described well with a single, dose-rate dependant, saturating exponential as proposed by the kinetic model from Kyoto [3]. The permanent damage that remains after a sufficiently long annealing period at room temperature is linear dependent on the total accumulated dose.

At the radiation levels investigated in this report the attenuation in the Ge-P-doped SM fibre shows neither evidence of saturation during irradiation nor of annealing after irradiation. The attenuation can be described by a single dose dependent term.

The overall attenuation for an optical connection between the tunnel and the SR surface building may be superior due to losses in the optical connectors (around 4 dB in total, i.e. 0.5 dB per connector) and radiation-induced degradation of the lasers or light emitting diodes [4].

7. ESTIMATE OF RADIATION INDUCED ATTENUATION IN THE LHC TUNNEL

To estimate the radiation induced attenuation in the tunnel we have used the fibre layout as presented in [1]. In point 7, communication fibres from the SR7 surface building reach low level electronic crates located under the cryostats in the tunnel by passing through the Long Straight Section, the Dispersion suppressors and the regularARC.

We consider here an optical fibre that connects a low-level electronics crate located under a cryostat at the mid ARC to an acquisition crate in the local control room in SR7. This fibre will be damaged by radiation from beamgas interaction in the ARC and from radiation due point losses in the Dispersion Suppressor and the Long Straight Section where the collimators are located. The dose rate in these areas during nominal operation have been simulated with cascade codes and the results can be found in [5] [6] [7] and [8] assuming the usual 200 days of LHC operation per year (4800 hours) at nominal intensity with fill durations of approximately 15 hours with 5-hour turnarounds.

Table III gives estimates of the radiation-induced damage in the 2 SM fibre types assuming that the attenuation depends only on the total accumulated ionizing dose. The overall attenuation for an optical connection between the tunnel and the SR surface building may be superior due to losses in the optical connectors (around 4 dB in total, i.e. 0.5 dB per connector) and radiation-induced degradation of the lasers or light emitting diodes [8].

Tunnel Area	Length [m]	Dose rate [Gy/h]	Annual Dose [Gy]	Attenuation 1310 nm Ge-P doped [dB/y]	Attenuation 1310 nm Ge doped [dB/y]
LSS R7	270	0.416	2000	42.0	5.4
DS R7	170	0.002	10	0.14	0.02
Half ARC	1214	0.001	5	0.49	0.06
Total	1654	-	3015	42.6	5.5

Table III. Estimates of the annual radiation induced attenuation in an optical fibre due to ionizing radiation around IR7 based on the fitting parameters in section 4 obtained from the 60Co gamma ray experimental data and the exposed fibre length in each tunnel area.

8. CONCLUSIONS & FUTURE WORK

The SM fibres in the LHC tunnel will show an increase in the attenuation of light at 1310 nm due to radiation damage from ionising radiation. The attenuation will depend on the wavelength of the light, the type and concentration of dopants in the Si-core, the total accumulated dose and the dose rate.

The observed attenuation in **Ge-P-doped SM fibres** irradiated at a dose rate of 500 Gy/hr is 0.08 dB/km per Gy for light at 1310 nm, which is approximately 8 times higher than that in Ge-doped SM fibres. The attenuation increases linear with the total dose and no saturation of the attenuation has been observed up to a total dose of 0.5 kGy. When the irradiation is stopped, Ge-P-doped SM fibres do not show any measurable short term annealing effect.

Ge-doped SM fibres show a saturating exponentially increasing attenuation at a high dose rate (1 kGy/hr) and the level of saturation is approximately 20 dB/km. There is a strong short term annealing when the irradiation source is turn off. At room temperature, the attenuation does not return to the level of the un-irradiated fibre. The remnant attenuation is approximately linearly dependent on the total dose and equal to 0.01 dB/km per Gy.
Draka performed blowing tests on 1km micro-ducts containing eight-fibre micro-cables. After irradiation up to 300 kGy the micro-cables could be blown in and out again at 100 meters per minute in test beds.

As a result of the work presented here Ge-P-doped fibres have been excluded from use in IR7 in favour of the more radiation tolerant Ge-doped fibres. In addition the routing of fibres has been optimized to minimize exposure in the hottest radiation areas and minimize attenuation. Fraunhofer INT has been commissioned to investigate, for different fibre types, the dose rate dependence of the attenuation increase and assess the impact of annealing at the time-scales of the LHC duty cycle.

References

[1] L. De Jonge, Presentation in the LHC Technical Coordination Committee, 6 December 2002, http://lhcp.web.cern.ch/lhcp/tcc/planning/tcc/Minutes/Mins2002/tcc2002-10/tcc2002-10.pdf.
[2] P. Borgermans, B. Brichard, , IEEE J. Trans. Nucl. Sci., Vol. 49, No. 3, June 2002
[3] M. Kyoto *et al*., IEEE Journal of Lightwave Technology, Vol 10, No. 3, March 1992.
[4] I.Azhgirey *et al*, LHC project note 297, CERN, June 4 2002.

RADIATION TOLERANT COMMERCIAL OF THE SHELF COMPONENTS FOR THE REMOTE READOUT OF RADFETS AND PIN DIODES

Authors:

C. Pignard, T. Wijnands, CERN Geneva 23 1211 Geneva Switzerland

Abstract

The radiation tolerance of a complete set of components required for the remote readout of Radfets and Pin diodes has been investigated. A radiation tolerant, temperature stabilized design for reliable remote readout up to 200 Gy in a complex field is discussed.

Geneva, October 2005

1. REMOTE READOUT OF RADFETS

1.1 Electric characteristics of RADFETs

Today, many different types of RADFETs exist and their response to photons or electrons can differ by an order of magnitude. For a remote readout device, the electric characteristics of the device need to be known in advance as it will determine the final inaccuracy and resolution of the on-line measurements. Of particular interest here are the initial voltage threshold, the temperature coefficient, the sensitivity and the readout current of the RADFETs (table I). All RADFETs presented here are commercially available from National Microelectronics Research Center (NMRC), Thomson and Nielsen Electronics Ltd. (T&N) or from REM Oxford Ltd. These manufacturers all propose RADFETs with different packaging and various gate oxides between 100 and 1000 nm thick (table I).

Manufacturer	NMRC	NMRC	NMRC	T&N	T&N	T&M	REM
Oxide	1000 nm	400 nm	100 nm	500 nm	250 nm	100 nm	940 nm
Type	300/50 W/L	300/50 W/L	300/50 W/L	TN502P	TN250P	TN100P	TOT502A-14
Readout Current	8.7 μA	8.7 μA	8.7 μA	100 μA	100 μA	100 μA	100 μA
Threshold voltage	5.43 V	1.57 V	2.72 V	5.49V	3.19 V	2.1 V	8.88 V
Temp Coefficient	-1.6 mV/ºC	-1.0 mV/ºC	-1.2 mV/ºC	-2.7 mV/ºC	-1.13mV/ºC	-0.66mV/ºC	-3.23 mV/ºC
Co-60 sensitivity	215 mV/Gy	65 mV/Gy	2.4 mV/Gy	38 mV/Gy	15 mV/Gy	3.4 mV/Gy	80 mV/Gy

Table I : Electric characteristics of commercially available (not irradiated) RADFETs from 3 different manufacturers.

Another important aspect is the readout protocol that is used to readout the RADFETs. There is no unique readout protocol for the threshold voltage despite the fact that the electrical properties of the RADFETs change during irradiation and that this may decrease the accuracy of the remote readings. It is usually recommended to read out the threshold voltage a few seconds after power switching and any current between 5 μA and 150 μA can be chosen. The readout protocol should not be changed during irradiation and one must assure that the current in the device has stabilized at the moment the threshold voltage is read. In the case presented here, a large number of RADFETs need to be read out on a regular basis and the time to readout a single RADFET should therefore be kept as short as possible. For the devices quoted in Table I, it was found that the current rise time increases with the gateoxide thickness and with the total accumulated dose (figure 1). The results presented in the remainder of this paper have been obtained reading out the threshold voltage at 10 ms after the power switching which assured a constant current for doses up to 200 Gy.

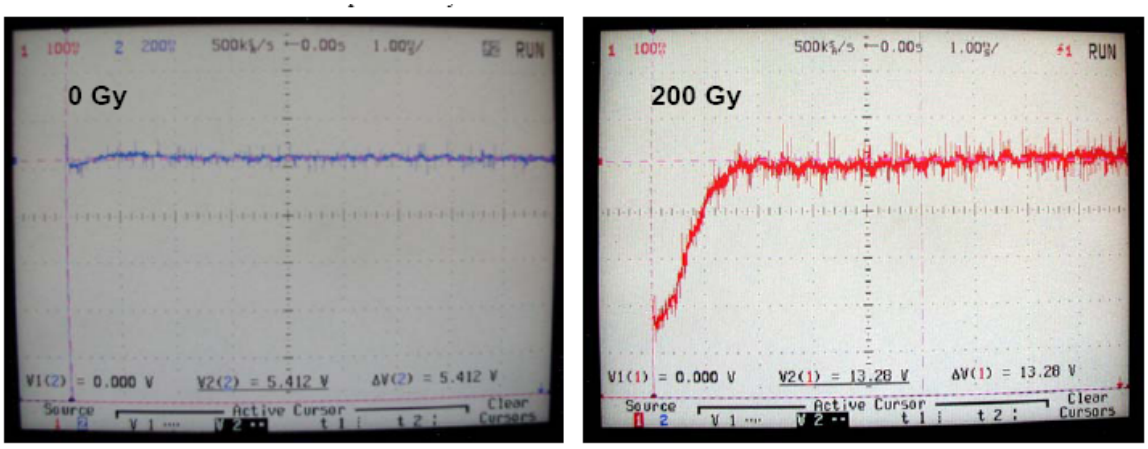

Figure 1: Variation of the current rise time of a TN502P RADFET from 0.01 ms (left) to 2 ms (right) after irradiation to a dose of 200 Gy .The time scale in the figures is to 1msec / square

The temperature coefficient of a RADFET varies as a function of dose accumulated and the total variation depends on the type of RADFET. For the 400 nm (300/50 W/L) and the 100 nm (300/50 W/L) RADFETs from NMRC for example, the temperature coefficients changed to -2.5 mV/ºC and -0.9 mV/ºC after 200 Gy (Co-60 irradiation). In practice, such variations can be fully thermo compensated (i.e less then a single bit error) provided the temperature variations are small (about 15 degrees maximum).

1.2 Schematic for remote RADFET readout

Figure 2 shows the logic and operating scheme for the remote RADFET readout. During irradiation, the RADFET is short circuited (switch S2 closed) and drain is connected to the source. To read out the RADFET, switch S2 is opened and a constant current is passed through the device. The threshold voltage is thermally compensated during the readout. The ADC is connected to the output register of a deterministic WorldFIP fieldbus interface.

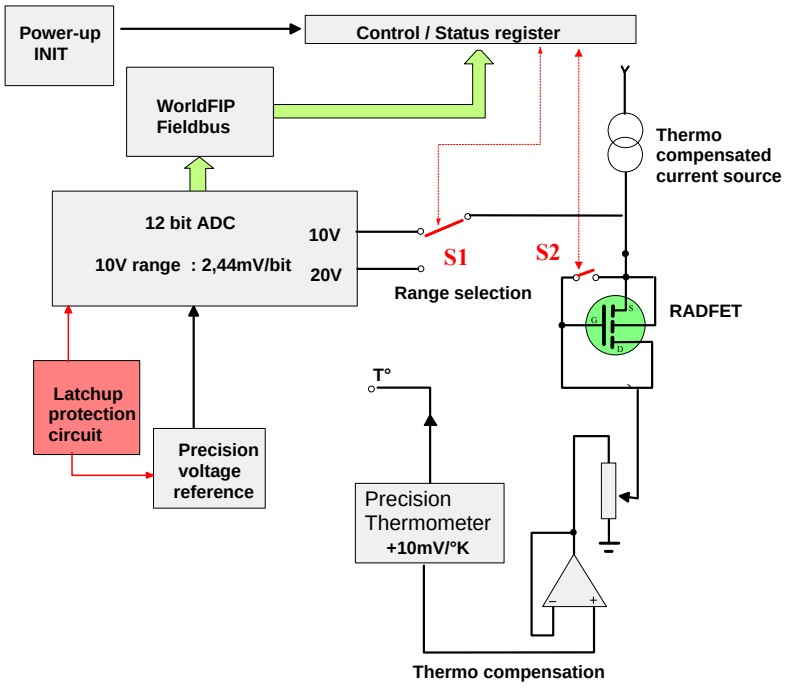

Figure 2 : Schematic for the remote readout of a RADFET using the WorldFip fieldbus interface.

1.3 Radiation tolerant components

One of the key components in the schematic in figure 2 is the thermo compensated current source. Any variation of the current from the source will influence the threshold or forward voltage reading of the associated radiation sensor. For the application discussed here, the LM234-Z3 from National [7] was used with a thermal compensation consisting of a si-diode and 2 resistors (figure 3, left). During irradiation up to 200 Gy (Co-60, 50 Gy/hr), the current drifted by 60 nA (figure 3, right). During the test, the temperature varied by 10 degrees and a thermal cycle after irradiation test confirmed that the thermo compensation of the source remained indeed fully operational.

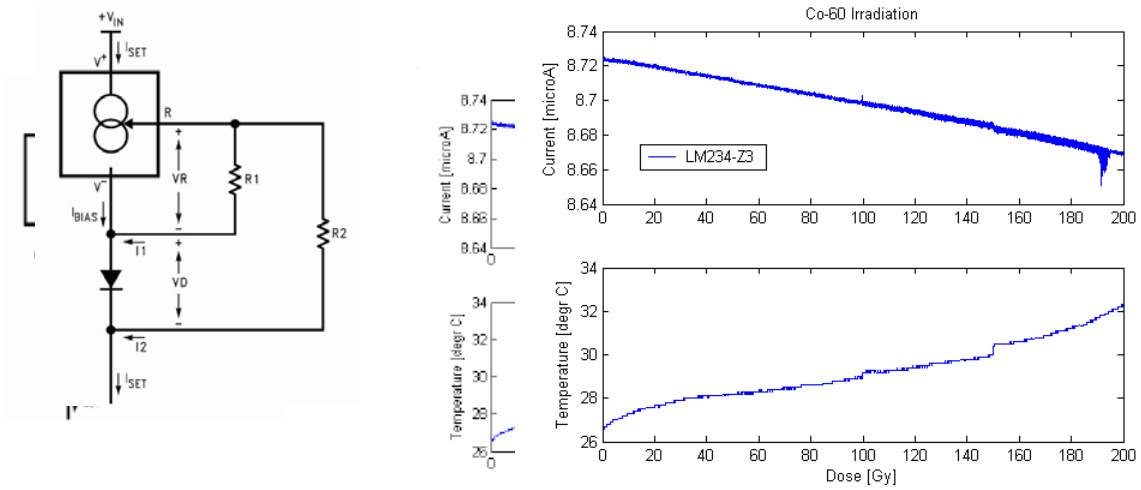

Figure 2 : (left) Details of the thermal compensated current source LM234-Z3 with a Si-diode BAS 16 from Infineon, (right) drift of the current source with total dose (Co-60, Dose rate 50 Gy/hr).

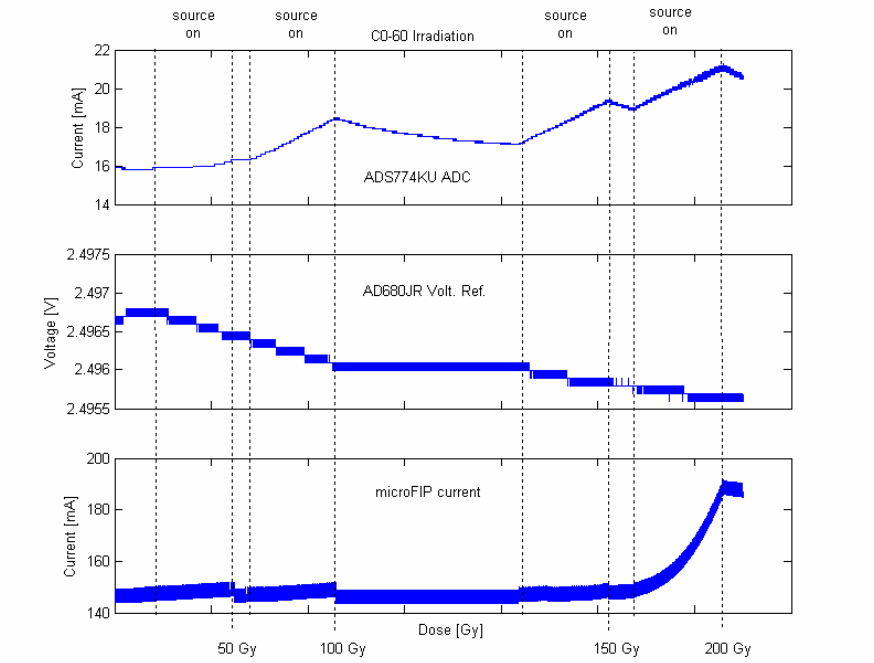

Figure 3 : (top) Current consumption of the ADS774KU A/D converter as a function of total dose, (middle) drift of the voltage reference (AD680JR) for the A/D converter (bottom) variation of the current consumption in the WorldFIP (microfip) fieldbus interface.

For the thermo compensation of the RADFET threshold voltage, a precision thermometer such as the LM35DZ (National) in combination with an operational amplifier OPA4234UA (Burr-Brown) may be used. These components did not show any significant degradation up to a total dose of 200 Gy. The 12 bit A/D converter ADS774KU from Texas Instruments was selected because this device showed no sensitivity to latch ups during an irradiation test in the LHC radiation test facility [6]. With an external 2.5 Volt voltage reference (AD680JR, Analog Devices), this device provides reliable ADC conversion at 100 Hz up to ~160 Gy TID. At 180 Gy the least significant could not be switched 'on' anymore and the S/N ratio had decreased by approximately 10%. At this point, the current consumption had increased by 30 % (figure 3, top). The external reference voltage (figure 3, middle) drifted by 400 ppm after a total dose of 200 Gy TID with no consequences for the operation of the ADC.

The 12 bit data is transmitted via a fieldbus bus interface (microFIP Philips VY27257, WorldFIP) which continues to operate correctly up to 200 Gy in a standalone operation mode with a bus access frequency of 0.1 kHz. This confirms earlier radiation tests on this device [8]. A Micrel MIC5203 linear voltage regulator can be used as a latchup protection circuit for the ADC as described in detail in [9].

Finally, two bilateral CMOS switches (TC4S66F, Toshiba) can be used to select the sensor and to short circuit the RADFET. Powered at 18 V, the TC4S66F is limited to a TID of 180 Gy whereas powered at 9 V it tolerance is 210 Gy. It is therefore important to have some prior knowledge on the maximum threshold voltage that can be expected from the RADFET.
The ADC, the control register and the VLSI chip are the only components in the schematic of figure 1 that are sensitive to SEUs. The risk of Single Event Error propagation can be mitigated by operating in "command-response" mode. As information on the dose and neutron fluence is permanently stored in RADFET and the pin diode, data does not need to be stored for a long period of time in the SEU sensitive components (maximum 100 micro seconds). In this operating mode, no SEUs were with a 60 MeV proton beam at an intensity of 1E8 protons/cm^2/s.

2. REMOTE READOUT OF PIN DIODES

The schematic in figure 1 can equally be used for the remote readout of neutron pin diodes such as the BPW34-FS (Siemens). This device has a temperature coefficient of -2.4 mV/ºC (not irradiated) and -3 mV/ºC (after 5x10^{12} 1 MeV n/cm^2) so that the forward voltage can be thermo compensated by same components as proposed for the remote readout of the RADFETs. The readout current for this diode is 1 mA.
In the layout shown in figure 1, it is also possible to read out several diodes in series thereby increasing the sensitivity. Due to increased temperature coefficient, the maximum number of diodes that can be read out at ZTC in the schematic shown in figure 2 is 3.

3. EXPERIMENTAL RESULTS WITH REMOTE READOUT

Reliable remote readout of RADFETs and pin diodes with components described above has been achieved in a pure gamma environment from Co-60 (figure 5, left) and in a mixed gamma-neutron field from a Uranium fission reactor (figure 5, right)

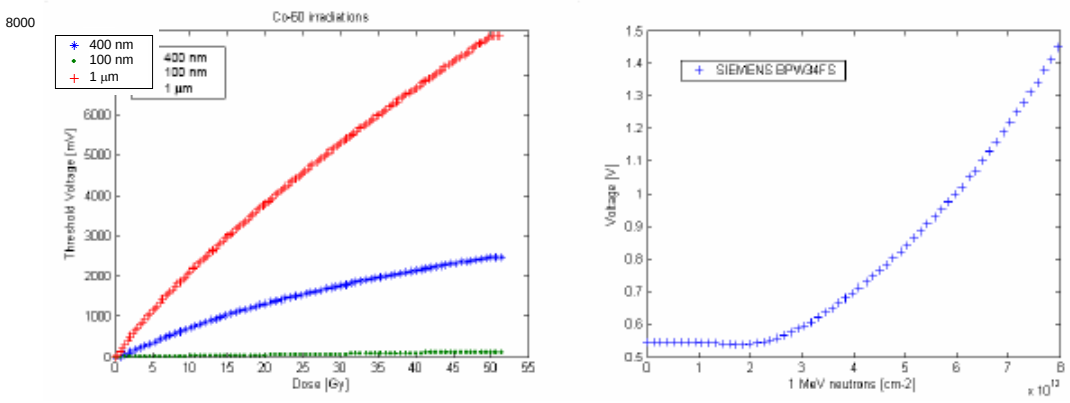

Figure 5 : (left) Threshold voltage shift in NMRC RADFETs from table I as a function of dose during C0-60 irradiation at 50 Gy/hr (right) Threshold voltage shift of a BPW34FS diode during irradiation with 1 MeV neutrons (neutron flux 2.88x10^{10} neutrons per cm^{2}s) from a Uranium fission reactor.

By reading out the voltage over a high precision resistance in parallel, it was confirmed that the observed change in the threshold voltage of the RADFET is entirely due to charge buildup in the gate oxide and not to any degradation of the readout electronics. During the 1 MeV neutron irradiation, the output of the Micrel MIC5203 linear voltage regulators showed a drift proportional to the fluence reaching 3% or 4% at 10^{13} 1 MeV neutrons. The output of the MIC5203 3.3 V voltage regulator for example, increased from 3.34 V to 3.45 V after $6x10^{12}$ neutrons at 1 MeV confirming earlier displacement damage tests on this component [

To validate the readout design for use in complex High Energy Physics (HEP) radiation environments, the remote readout was irradiated in the LHC irradiation test facility at CERN [11]. The complex radiation field in this facility is generated by a 450 GeV proton beam that hits a primary target and creates a hadronic cascade. In the area behind the target, the dose rate is approximately 12 Gy/day and the fluence to dose ratios are $8x10^{10}$ neutrons/Gy (1 MeV equivalent neutrons), $4x10^{9}$ hadrons/Gy (20 MeV or higher) and $2x10^{9}$ hadrons/Gy (100 MeV or higher).

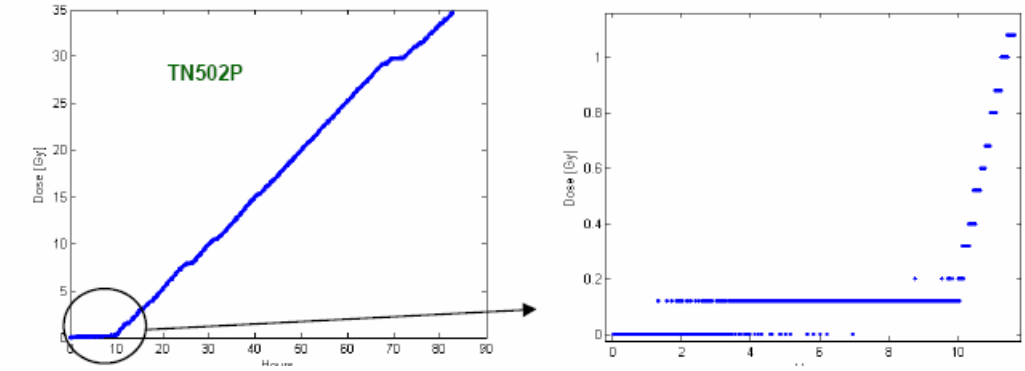

Figure 6 : (left) Remote on line measurements of the dose with a TN502P RADFET from Thomson and Nielsen exposed in High Energy Physics radiation field (right) Zoom of the first few hours of exposure in the facility showing the feasibility of using the remote readout to monitor remnant dose rates (the remnant dose rate in this example was approximately 1 mSv/hr).

Figure 6 shows the dose measurement as a function of time. During the first 10 hrs, there is no beam on target and the RADFETs measure the remnant dose from the activated beam dump. When the proton beam is on, the dose rate increases by approximately 3 orders of magnitude as visible by the detailed figure on the right (figure 6, right). The remote readout continued to function correctly up to a total dose of 160 Gy confirming earlier radiation tests with mono energetic single type particles.

REFERENCES

[1] A. Holmes-Siedle, "The space-charge dosimeter", Nucl. Instr. and Methods vol 121 pp 169-179, 1974.

[2] A. Holmes-Siedle, L. Adams, "RADFET : a review of the use of Metal Oxide siliscon devices as integrating dosimeters", Rad. Phys. Chem. vol 28 pp 235-244, 1986.

[3] A. B. Rosenfeld *et al*, "PIN diodes with a wide measurement range of fast neutron doses", Rad. Prot. Dos. 33 No1/4 (1990) 1375-1379

[4] T. Wijnands et al, "Radiation Monitoring for the LHC machine", CERN 4th Annual Radiation Workshop, CERN Geneva, Switzerland, December 2004 http://agenda.cern.ch/fullAgenda.php?ida=a044378

[5] T. Wijnands, Proc of the 7th European Conf on Radiation and its effects on Comp. and Systems, RADECS 2003

[6] http://documents.cern.ch/cgi-bin/setlink?base=lhcnot&categ=Note&id=project-note-235

[7] http://www1.jaycar.com.au/images_uploaded/LM134.PDF

[8] M.A. Rodriguez-Ruiz et al., LHC Project Report 503, 17 October 2001.
http://lhc-radwg.web.cern.ch/LHC-radwg/Publications/Cryogenic_System/SEU_Tests_on_DCS_for_LHC_Cryo.pdf

[9] http://atlas.web.cern.ch/Atlas/GROUPS/DAQTRIG/DCS/ELMB/DOC/elmbseeprotection.pdf

[10] http://elmb.web.cern.ch/ELMB/nielreport11-03.pdf

[11] C. Fynbo et al, LHC Project Note 235, September 2000, CERN.

RADIATION INDUCED EFFECTS ON THE SENSORS OF THE HYDROSTATIC LEVELING SYSTEM FOR THE LHC LOW BETA QUADRUPOLES

Authors:

E. Dimovasili, A. Herty, H. Mainaud Durand, A. Marin, F. Ossart , T. Wijnands

Abstract

The response of the Hydrostatic Leveling System (HLS) for the final focusing quadrupole magnets in the Large Hadron collider is dose rate dependent. At high dose rates, ionization of the air inside the sensors causes charge deposition and this perturbs the position measurement. A model is presented that corrects the HLS signal offset as a function of the dose rate.

Keywords: LHC, Low beta quadrupoles, alignment, HLS, radiation, ionization

Geneva, October 2005

1. INTRODUCTION

The Large Hadron Collider (LHC) [1] is a 7 TeV energy proton collider under construction at CERN. The aim of this machine that will become operational in 2007 is to inject, accelerate and collide two proton beams of 10^{11} particles. At the interaction points large detectors will detect the collision products. A very important performance parameter is the luminosity which is proportional to the number of collisions per second and for the LHC it will reach the value $10^{34}cm^{-2}$ s^{-1}. In order to achieve this goal, it is required to focus the two beams -before collision- using 3 quadrupole magnets, the so called inner triplet. The size of the beam is very small and therefore the alignment of the magnets in the inner triplet is very important, concerning both their relative position with respect to the detector and with respect to each other.

The Hydrostatic Leveling System (HLS) will provide relative measurements of the vertical magnet position and its transverse tilt. The sensors of the HLS system have to operate reliable in a complex radiation field, as at their location (under the cryostat of the low beta quadrupoles) there is a strong radiation field with dose rates up to 16,000 Gy/year.

During previously conducted aging tests with 60Co, it was found that the HLS sensors show a strong dependence on the dose rate. In this paper, it will be shown that the charge produced by radiation in the air cavity of the HLS, is deposited on the surface of a capacitance and interpreted by the read- out electronics as a movement of a magnet. This offset can be corrected with the data provided in this paper.

2. HYDROSTATIC LEVELING SYSTEM

2.1 Operating principles of the HLS

The basic principle of the HLS system consists in measuring the water levels in a closed circuit. The systems that are used for the particle detectors of the LHC are composed of one hundred hydrostatic sensor units [2] interconnected with fluid and air pipes and located in referenced points onto the final focusing quadrupoles. The HLS along with a cross section are shown in Figure. 1.

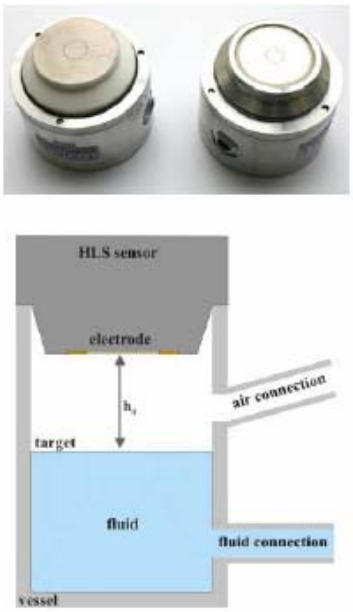

Figure 1: (upper) Two different HLS sensors, (lower) a cross section of a HLS sensor.

The HLS sensors perform hydrostatic leveling measurements with respect to a plane which is the free surface of a water network following the principle of communicating vessels. The continuous monitoring of the relative position is performed by the sensor's surface (electrode) and the water surface (the target). The electrode and the target are separated by air. The electrode is integrated in the top of the vessel. The principle of operation is based on capacitive measurements that determine the distance to the target. When a voltage is applied to one of the plates, the difference between the charge stored on the surfaces of the plates will cause an electric field to exist between them. The amount of existing charge determines the amount of current required to change the voltage on the electrode.

The driver electronics continuously change the voltage on the electrode with an excitation frequency of 4 kHz. The amount of current required to change the voltage on the electrode is detected by the electronics and indicates the amount of capacitance between sensor and target. The change ΔC in capacitance is directly related to the change in the distance between the electrode and the target level [3] as:

$$\Delta C = \frac{\varepsilon_o \cdot \varepsilon_r \cdot S}{\Delta h} \qquad (1)$$

where ε_0 the absolute permittivity of free space (8.85×10^{-12} F/m), ε_r the relative permittivity (dielectric constant) of air, S the surface of the electrode and Δh the variation of the distance between the electrode and the target.

The resulting output voltage is given by equation (2) [3]

$$V_{out} = (V_{offset} + \frac{1}{C_e} \cdot V_e \cdot C_{ref}) \cdot G \qquad (2)$$

2.2 Radiation induced effects

The physical process inside the sensor is assumed to be similar to those inside an ionization chamber. The Bragg Gray principle is applied here [4], which states that the absorbed dose in a given material can be estimated from the ionization produced in a small gas-filled cavity within the material. This principle is valid because the secondary electron ranges are long compared to the internal dimensions of the HLS chamber.

Ionizing radiation creates ions and electrons in the air between the electrode and the target. In the presence of the applied potential difference, the ions and electrons move in opposite directions. The charge deposited by the particles on the target plate changes the electric field and varies the excitation voltage. The more the ionization, the more the charge produced and collected on the electrode. The amount of existing charge determines how much the voltage has to vary so as to keep the electric field between the electrode and the target stable. Since some charge is already produced by radiation, the system needs to make less 'effort' to charge the electrode. At low dose rates, the amount of electron-ion pairs produced in the air between the target and the water level is proportional to the dose. At higher dose rates, more positive and negative ions recombine so that the signal of the HLS eventually saturates. The dose rates to the sensors are high and ions are uniformly distributed in the air cavity [5], therefore it is assumed that general recombination is the dominant effect.

2.3 Experimental set –up

Three HLS sensors were irradiated with gamma rays from a ^{60}Co source. Two different types of HLS were used: the H7D5-361 with a ceramic electrode (1st generation) and the H7D5-372 and H7D5-001, both with a glass electrode (4th generation).

The irradiation was done at different distances from the source so as to vary the dose rate. Measurements were performed at the dose rates 50 Gy/hr, 100 Gy/hr, 500 Gy/hr, 100 Gy/hr and 1500 Gy/hr. The measurements were repeated once at the same dose rates but with descending order, i.e from 1500 Gy/hr to 50 Gy/hr. The HLS electronics were switched on 4 hours before the first irradiation session, for the signal to stabilize. The vacuum pump system was also installed outside the hall in order to be able to perform tests in parallel. The temperature in the hall remained constant within 10 degrees of Celsius.

2.4 Experimental results

The variation of the output voltage as a function of the dose rate is shown in Fig. 2. The experimental data for all the sensors are plotted along with an average exponential growth polynomial. The shape of the curve indicates the existence of recombination in the sensor.

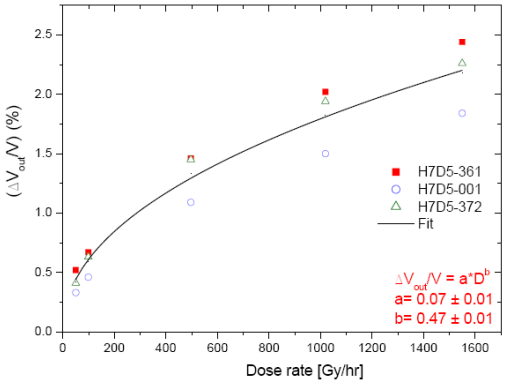

Figure 2: The measured voltage offset for all sensors and the average variation (in black).

It was initially assumed that the HLS sensors show a similar response with condenser ionization chambers [5]. This allows the calculation of the ionization current by the following equation [7]:

$$I_{ion} = \frac{\dot{D} \cdot m \cdot S_g}{W \cdot S_W} \qquad (3)$$

where is the dose rate in the air inside the sensor, I_{ion} the induced ionization current, m the mass of air inside the sensor, S_g/S_w the ratio of the mass stopping power of the gas and the wall and W a constant that depends on the gas and it has the value 34.1 J/C for air.

This current was calculated assuming that it is a dc current, that the electric field remains constant and that it can be added to the one flowing in the circuit. In this case, the ionization current induced in the sensor at all different dose rates was calculated and it is given in Table 1. The fourth column is the relative output voltage reduction $\Delta V_{out}/ V$, (ΔV_{out} is the difference between the sensor's signal during irradiation, V^{rad}_{out}, and the sensor's signal before the irradiation, V_{out} , i.e.

$$\Delta V_{out} = V^{rad}_{out} - V_{out}t \qquad (4)$$

In order to verify that the ionization current I_{ion} is linked to the variation of the output voltage of the HLS sensor, the relative voltage reduction was calculated by equation (2). The results are given in Table 1.

Table I:
THE IONIZATION CURRENT AND THE VOLTAGE DECREASE
IN THE HLS SENSORS AT VARIOUS DOSE RATES

Sensor	**Dose rate [Gy/hr]**	I_{ion}	$\Delta V_{out}/V$ (%) (meas)	$\Delta V_{out}/V$ (%) (calc)
H7D5- 361	50	0.50	0.52	0.46
	100	1.00	0.67	0.60
	500	4.98	1.46	1.29
	1000	10.31	2.02	1.79
	1500	15.65	2.44	2.16
H7D5- 001	50	0.77	0.33	0.29
	100	1.53	0.46	0.41
	500	7.64	1.09	0.98
	1000	15.83	1.50	1.34
	1500	24.03	1.84	1.65
H7D5- 372	50	0.50	0.41	0.36
	100	1.00	0.63	0.56
	500	4.98	1.45	1.28
	1000	10.31	1.94	1.72
	1500	15.65	2.26	2.00

Table 1 shows that the ionization current (I_{ion}) is not linearly proportional to the offset ΔV_{out}. This verifies the existence of recombination in the HLS sensors. The ionization current versus the measured output for all different dose rates is shown in Fig. 3 along with exponential growth fits of first order. The errors are less than 0.1% in all cases and they do not appear on the plot.

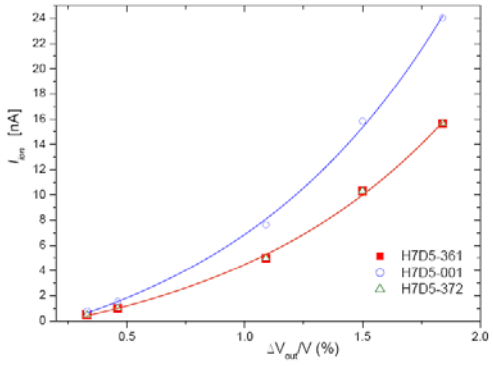

Figure 3: Ionization current versus output potential difference for all sensors. The lines are exponential growth fits of first order.

3. DISCUSSION AND CONCLUSIONS

The signal from the sensors for the Hydrostatic Leveling System of the LHC will be modified when exposed to ionizing radiation. The radiation induced charge is accumulated on the capacitor plates and provokes a voltage variation in the sensor which is operated at a constant electric field. By assuming a constant ionization current, the HLS can be compared to a condenser type ionization chamber. This model is in good agreement with the experimental data and can be used to predict the HLS offset at arbitrary dose rates. It was found that the charge on the electrode is increasing due to ionization in the air inside the sensor and therefore the voltage that is needed to maintain the electric field is reduced. This is interpreted by the electronics as a capacitance change and the output voltage decreases. In other words this effect is due to the electronics design rather than a real 'internal movement' of the HLS sensor and it explains the fact that the offset is observed only during the exposure of the HLS to radiation.

In addition, the experiments at Saclay have shown that the HLS sensors do no show any signs of aging. The radiation resistance of the HLS electronic readout is approximately 200 Gy Total Ionising Dose and comparable to standard Commercial Of the Shelf Components. During the LHC operation, the HLS may show radiation induced offsets of the order of a few microns. The signal of the HLS can be corrected with a model based on the study provided here.

The HLS will be installed on the external metrological reference points of the low beta quadrupoles of the LHC, in a very high radiation environment. Rough estimates of various radiological parameters associated with the inner triplet of the high luminosity insertions of the LHC can be found in [8, 9]. The HLS will have to resist dose rates up to 10 Gy/hr for the first year of the LHC operation. Such dose rates will have no effect on the lifetime of the HLS but they will provoke an offset of about 10 microns to the HLS reading.

REFERENCES

[1] LHC Design Report, Volumes I- III, CERN.
[2] http://www.fogale.fr
[3] F. Ossart, Fogale Nanotech [private communication]
[4] Attix F.H., Roesch W.C. and Tochilin E., 'Radiation Dosimetry, II; 9. Academic Press, New York (1966).
[5] J. W. Boag, The Dosimetry of Ionizing Radiation, edited by K. R. Kase B. E. Bjarngard, and F. H. Attix, Vol. 2 Chap. 3, Academic Press, Orlando, (1987).
[6] H. Vincke, SC-RP, CERN (private communication).
[7] J. Turner 'Atoms, Radiation and Radiation Protection' Eds J. Wiley & Sons Inc, 2nd Edition, (1995).
[8] M. Huhtinen and G.R Stevenson, Energy deposition, star densities and shielding requirements around the inner triplet of the high luminosity insertions of the LHC, CERN Divisional Report TIS-RP/IR/95-16 (1995), LHC Note 338.
[9] M. Huhtinen and G.R Stevenson, Estimates of dose to Components in the LHC Tunnel close to the Quadrupoles of the High- luminosity Low- beta regions, LHC Project Note 22.

DOSIMETRY ASSESSMENTS IN THE IRRADIATION FACILITIES AT THE CERN-PS ACCELERATOR

Authors

M. Glaser, F. Ravotti, *Student Member, IEEE* and M. Moll

Abstract

At the CERN Proton Synchrotron (PS) accelerator complex, two experimental zones allow the irradiation of samples in a 23 GeV pure proton beam and in a secondary particle environment dominated by 1-MeV neutrons and gamma rays. In this paper a review of the operative irradiation systems named IRRAD1 and IRRAD2 is presented, as well as the improvements in the techniques used for the beam characterizations and dosimetry.

Keywords: Accelerators, Dosimetry, Neutron beams, Proton beams, Radiation Monitoring.

Geneva, October 2005

1. INTRODUCTION

In THE experiments of the future CERN Large Hadron Collider (LHC) [i], all materials, optical and electronic components, as well as the particle detectors themselves will be exposed to a harsh radiation environment constituted of electromagnetic and hadronic radiation.

To study radiation damage in semiconductors and other electronic devices [ii], since 1998 two irradiation facilities are operated in the East Hall Experimental Area of the Proton-Synchrotron (PS) accelerator at the European Organization for Nuclear Research (CERN) [iii], [iv]. The facility named IRRAD1, located in the PS-T7 beam-line, allows irradiation experiments with the 23 GeV primary proton beam. The IRRAD2 facility, located at the end of the PS-T8 beam line, allows irradiations in a mixed neutron/gamma-ray environment (mainly neutrons of about 1-MeV) produced in a cavity before a beam stopper.

Over the last few years the number of irradiation experiments performed annually at these facilities, as well as their complexity, has considerably increased. Experimental assemblies that need on-line readout and experiments performed with non standard beam conditions (high and low intensity, different beam size, special setups for SEE testing, etc.) are performed more and more frequently. Some examples are given in Ref. [v] and Ref. [vi]. Along with these experiments comes the request for a more precise characterization of the beam profile, the beam intensity and the particle composition of the radiation field. To satisfy these demands, the facilities and the used dosimetry techniques are in a constant evolution. Recently the facility control system has been fully automated and the radiation levels in the irradiation zones are measured on-line. The radiation level data are stored together with information regarding the object under irradiation as well as the beam conditions in an on-line database that allows to keep track of all irradiated material [vii].

In the year 2004 about 1200 objects have been irradiated. The dosimetry is mainly performed by the activation of Aluminum foils; however techniques like the use of Gafchromic and OSL based films for beam profiling are extensively employed. Measurements with Silicon Radiation Detectors, RPLs, PADs and RadFETs for NIEL and IEL measurements have also been further developed. A part of this developments is performed in the framework of the CERN-RADMON Working Group [viii] which has the task to provide the LHC machine and the five LHC experiments with radiation monitoring devices.

In this paper we briefly describe the layout and operation of the irradiation facilities (Section II) and then focus on the different techniques used for the characterization of the proton beam (Section III) and the neutron environment (Section IV). Finally, in Section V, the safety issues concerning the irradiated materials at the CERN PS are addressed.

2. CERN-PS IRRADIATION SYSTEMS

In the T7 beam-line the primary 23 GeV proton beam of the PS accelerator is directed to the irradiation area where the facility named IRRAD1, a remote controlled shuttle system, is located. In this zone the proton bursts are delivered during the 15s-supercycle of the PS machine in 1-3 spills of about 400 ms each (slow extraction) with a maximal beam intensity of $2x10^{11}$ protons per spill. A defocusing-scanning system is used to spread out the beam in order to produce a uniform irradiation spot over a surface that can vary from 2 to 25 cm^2 [iii]. Changing these two parameters, proton fluxes from $8x10^{11}$ $cm^{-2}{\cdot}h^{-1}$ to $8x10^{13}$ $cm^{-2}{\cdot}h^{-1}$ can be achieved.

The IRRAD1 shuttle moves on a rail inside a metal conduit of a length of about 15 m and allows to place the samples to be irradiated directly from the counting room into the irradiation area. The conduit is inserted into a radiation shielding constituted of concrete blocks as shown in Fig. 1. In the irradiation location, to decrease the neutron backscattering to a few percent, a marble absorber of 20 cm has been inserted between the shuttle position and the following iron beam stopper.

A luminescent screen with a camera is used do display the beam spot and a Secondary Emission Chamber (SEC) [ix] provides a measurement of the total beam intensity during irradiations.

Figure 2 shows the layout of the irradiation zone IRRAD2 located at the end of the T8 beam-line. The irradiation is performed in a cavity with secondary particles produced by the primary 23 GeV proton beam after crossing a target constituted of 50 cm of carbon and 5 cm of lead [iii].

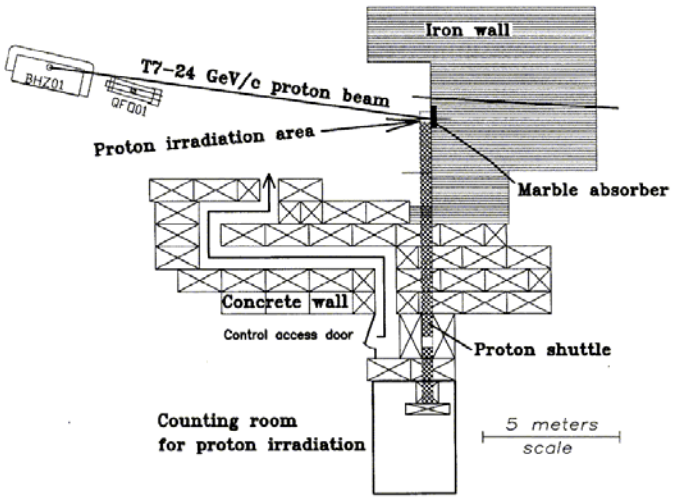

Figure. 1: Layout of the IRRAD1 Irradiation Facility.

As for the IRRAD1 facility, a motorized shuttle system allows to transport the samples from the counting room to the irradiation cavity in which a broad spectrum of neutrons, gamma rays and charged hadrons is produced. Fig. 3(a) shows the typical spectrum obtained by Monte Carlo simulations with the FLUKA code [x], while in Fig. 3(b) the three dimensional particles profile inside the irradiation cavity is shown. The secondary particles intensity into the IRRAD2 cavity of Fig 3(b) has been measured by means of activation foil technique.

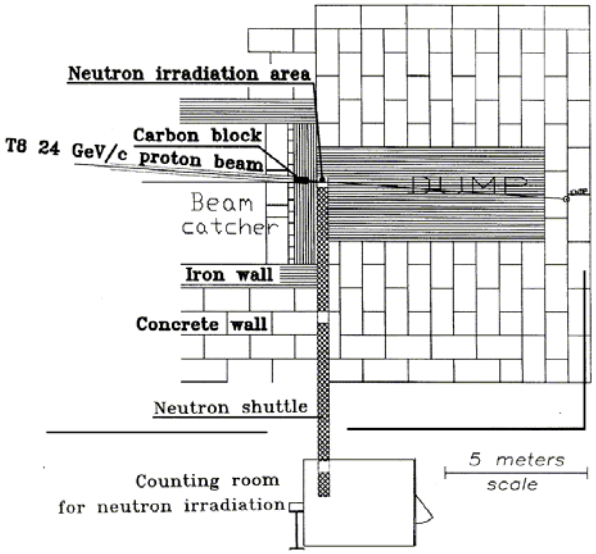

Figure 2: Layout of the IRRAD2 Irradiation Facility.

With the remote controlled shuttle system it is possible to set the position of the samples in the vertical coordinate Z with respect to the beam axis. Depending on the position Z, the ratio of charged hadrons in the GeV energy range to neutrons and gammas can be chosen. It is thus possible to perform irradiations in a pure gamma/neutron environment (at positions far from the beam axis, typically Z = 50 cm) or in a charged-hadron rich radiation environment that better represents the one expected for the inner detectors of the LHC experiments (at positions close to the beam axis, typically Z = 10 cm).

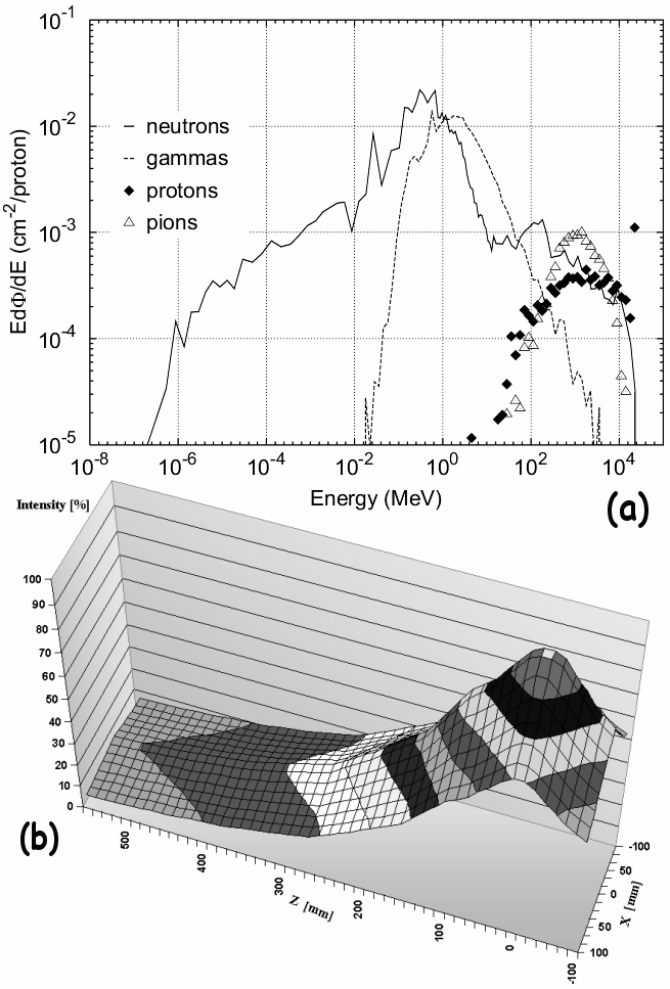

Figure 3: Particle spectra in IRRAD2 cavity at 10 centimeters from the beam axis normalized to one impinging 23 GeV proton (a) and particle profile as measured by the Al activation method in the IRRAD2 cavity in function of the distance from the beam axis Z (b).

The proton bursts delivered in the T8 beam-line have the same time-structure as those of the T7 beam-line. It is therefore possible to reach 1-MeV neutron equivalent fluxes from 0.3 $cm^{-2} \cdot h^{-1}$ to $1x10^{12}\,cm^{-2} \cdot h^{-1}$ depending both on the number of spills delivered by the PS and the distance of the sample from the beam axis. A Secondary Emission Chamber (SEC) [ix] provides finally a measurement of the primary proton beam intensity that hits the target.

3. PROTON BEAM CHARACTERIZATION AND DOSIMETRY

3.1 Activation Measurement of Aluminum Foils

The basic measurement performed on the 23 GeV proton beam is the determination of the proton fluence by evaluating the ^{24}Na and ^{22}Na activity of Aluminum (Al) foils produced via the nuclear reactions ^{27}Al(p,3pn)^{24}Na and ^{27}Al(p,3p3n)^{22}Na respectively [xi]. With these activation techniques it is possible to obtain fluence measurements with an accuracy of ± 7 %. The size of the aluminum foils with a thickness of some hundred □m is varying from 0.5 to 2 cm^2 according to the size of the samples that have to be irradiated. The half-lives of ^{24}Na and ^{22}Na are about 15 hours and 2.6 years, respectively. According to the time elapsed after irradiation and the irradiation time itself one of the two isotopes is chosen to be measured for the fluence calculation.

Taking into account that ionization is the main contribution to the energy loss of a charged particle and that its mean value, the stopping power (dE/dx), is given by the Bethe-Bloch law, it is possible to simply convert the fluence into the dose (Gy) deposited in thin samples, using the following formula:

$$D = K \times (dE/dx)_m \times \Phi \qquad (1)$$

where □ is the proton fluence expressed in particles/cm^2, K = 1.602x10^{-10} is a scale factor, and $(dE/dx)_m$ expressed in MeV•cm^2/g, is the minimum ionizing energy loss rate. For 23 GeV protons it has values between 1.6-1.8 MeV•cm^2/g for materials that are typically irradiated in the facilities. For high-energy charged particles, the contribution of nuclear interactions and the resulting secondaries to the dose in the beam is usually small and can thus be neglected under normal circumstances [xii].

Apart from the above described fluence measurements, the beam is also characterized with different types of Gafchromic sensitive medias (Gafchromic is a registered trademark of ISP Corporation) [xiii] and thin Optically Stimulated Luminescence (OSL) films when a detailed determination of the dose map over the irradiation surface is needed [xiv].

3.2 Gafchromic Dosimetric Films

Gafchromic Dosimetric Films XR, Type-R, HD-810 and MD-55 [xiii], are currently used for beam profiling, alignment and dose measurements before and during sample irradiation. The films develop a characteristic color upon exposure to ionizing radiation and become progressively darker in proportion to the absorbed dose.

The high sensitivity of the Gafchromic XR Type R film allows an accurate measurement of the proton beam position with a few spills of particles only. The time consumption in the alignment of the IRRAD1 shuttle is thus considerably reduced with respect to the previous procedure which used thin pieces of glass that darkened only after a considerable higher number of proton spills (≈250). The films Gafchromic MD-55 and HD-810 are transparent media in which the active layer is coated on thin transparent polyester layers. They develop a characteristic blue color after exposure that can be measured by means of a transmission densitometer. The color density is thus used to measure the absorbed dose during irradiation. Several samples of 1 square centimeter were irradiated in IRRAD1 to obtain the calibration curve shown in Fig. 4 that correlates the color Net Density (N_D) with the absorbed dose.

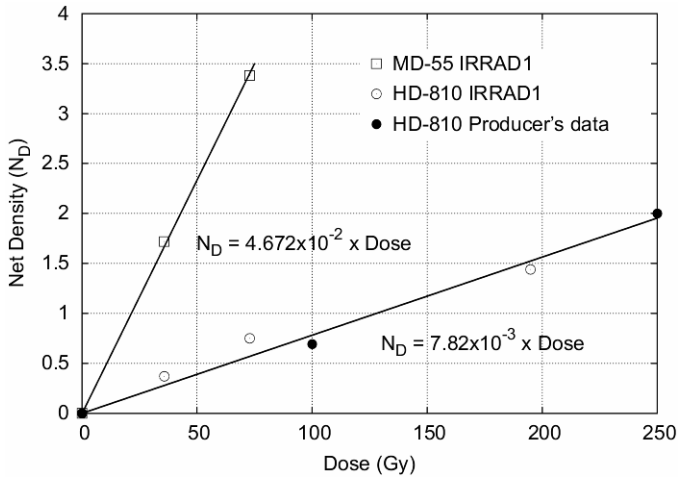

Figure 4: Gafchromic Dosimetric Films HD-810 and MD-55. Calibration curves obtained in IRRAD1 facility compared with producer data.

The films were wrapped in a layer of aluminum foil to facilitate handling and irradiated at varying fluences to produce doses from 10 Gy to more than 1 kGy. The optical density of both film types increases with time reaching saturation less than 24 hrs after irradiation. Hence, the readings were performed after such time for the present calibration [xv]. The change in optical density of the films was measured using a *Nuclear Associates Model 37-443* Densitometer. Unexposed samples were used to provide a base optical density, which was subtracted from the measured one for the N_D calculation.

3.3 Optically Stimulated Luminescent Materials

The film used for Optically Stimulated Luminescent (OSL) dose mapping is a 100 □m thick layer of doped Strontium Sulfide (SrS), silkscreen printed on a kapton foil. After beam exposure, the OSL exhibits a visible emission spectrum when stimulated with near infrared light [xvi], [xvii]. The OSL foil reader is a solid-state laser beam (of about 1.0 □m wave length) focused on the irradiated foil that is positioned on a X-Y stage [xviii]. The laser beam is stepped over the foil in the two axes and the emitted luminescent signal (of about 600 nm wave length) is collected by means of a photo-multiplier tube.

Finally the signal is digitized and recorded to get a map of the emitted luminescence versus X and Y-axis that represents the beam profile. After reading, the material can be completely reset by a 24 hour annealing at 80°C. The films used at the irradiation facilities were designed to measure doses in the range 0.1 – 100 Gy.

Their spatial resolution is strongly depending on the dimension of the laser spot used for the readout. With the test bench available in the laboratory of the CEM^2 at the University Montpellier II, France it is possible to obtain maps of the proton beam with a 250 □m resolution like the examples shown in Fig. 5.

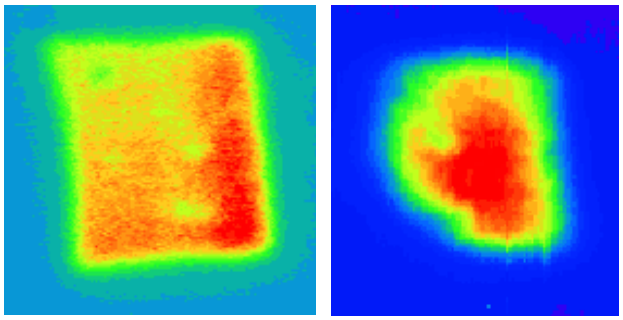

Figure 5: High-resolution beam profiles measured by a 100 □m OSL film. Big beam-spot of about 4.5 x 4.5 cm^2 (left hand side) and standard beam spot of about 2 x 2 cm^2 (right hand side).

3.4 Secondary Electron Emission from thin metal foils

The need for an on-line method to determine the position and the profile of the PS-T7 proton beam motivated a feasibility study of an instrument based on the proton-induced Secondary Electron Emission (SEE) from thin metal foils [[xix]]. The foils are required to be made of a low cost and relatively short activity lifetime material. Moreover they have to be on the one hand thin to avoid scattering of beam but on the other hand thick enough to allow easy handling. Aluminum foils were chosen as a good compromise to satisfy most of these requirements. A test setup was realized to verify our calculations and to perform a proof of principle before starting the design of a full Beam Profile Monitor (BPM) system.

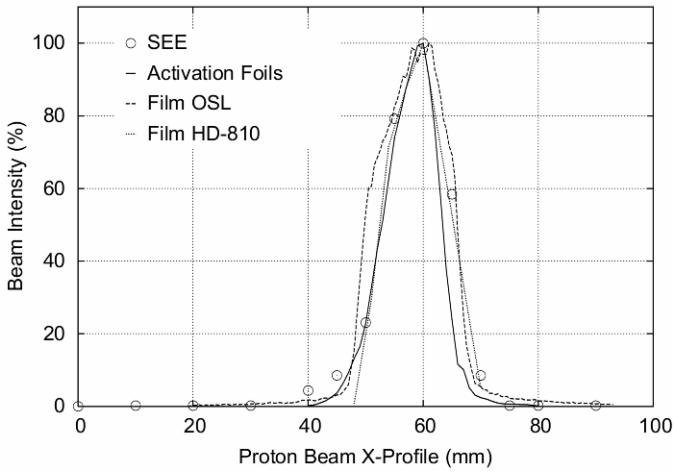

Fig. 6. BPM measurements (circle marks) compared with the profiles obtained by means of OSL, activation foils and Gafchromic Films (different continuous lines)

The BPM test setup consisted of a 3x3 cm^2, 100 □m thick aluminum foil mounted transversally on the IRRAD1 shuttle allowing the beam to pass through the full 3 cm width of the foil. The foil was electrically connected to a high-gain Transimpedance Amplifier located in the counting room via a 15-meter long coaxial cable. The amplified signal was read out with a *LeCroy 9361* 300 MHz Oscilloscope. At a fixed vertical position the foil was displaced to different horizontal positions ranging from 0 to 90 mm and the charge integrated over one particle spill was measured at each step in order to get a horizontal profile.

Fig. 6 shows the obtained results (circle marks) normalized with respect to the maximum intensity of the beam spot and compared with the same measurement obtained by the profiling techniques mentioned above (various lines). The good agreement of the measurements and the high current collected from the Al foil (a few nA in the center of the beam spot) allows now to proceed with the project by designing a multi-pad detector.

4. DOSIMETRY IN THE MIXED GAMMA/NEUTRON ENVIRONMENT

Different dosimetry techniques are used to monitor the neutron fluence and the deposited Total Ionizing Dose (TID) in this complex environment depending on the irradiation position and upon the specific user request. For radiation hardness tests and solid-state device characterizations, the environment at 50 cm distance from the beam axis is often privileged. In this position the radiation field is composed mainly of 1-MeV neutrons (90 %) with a small gamma ray contamination (10 %). Fig. 7 shows the detail of the particle spectra in this location.

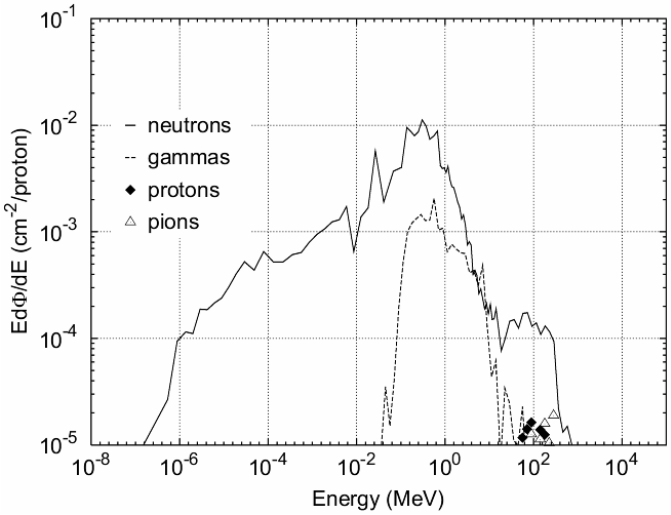

Figure 7: Particle spectra in IRRAD2 cavity at 50 centimeters from beam axis normalized to one impinging 23 GeV proton.

Calculations based on simulations and activation-foil techniques [xx] as well as measurements with Polymer-Alanine Dosimeters (PAD), Radio-Photo-Luminescent glasses (RPL) [xxi], Gafchromic films and Silicon detectors [xxii] were carried out for the calibration of the location at 50 cm distance from the beam axis. Samples of each dosimeter type were irradiated to 10 different neutron fluences.

Monte Carlo simulations with the FLUKA code have been carried out to predict the hadron flux and the production of ^{24}Na in a thin Al foil placed at 50 cm from the beam axis. The expected delivered dose in the Aluminum, normalized to one proton hitting the target, has also been computed. Measuring the ^{24}Na activity allows therefore to calculate the achieved particle fluence in terms of 1-MeV neutron equivalent fluence (Φ_{eq}).

Fig 8 shows the production rate of ^{24}Na per incident proton predicted by simulations in 20×20 cm^2 Al foils (continuous line) compared with the measurements carried out with Al foils placed at different distances from the beam axis ranging from Z = -70 cm to Z = +20 cm. The measurements (light dotted lines) taken at steps of 5 cm with foils of 1×1 cm^2, have been normalized to the 20×20 cm^2 area (dark dotted line) to allow the comparison with the simulation output. The two sets of ^{24}Na production rates turn out to be in agreement within 20 % for all the irradiation positions (i.e. distances from the beam axis). In all the cases the measured ^{24}Na production overestimates the corresponding simulated values by about 20 %.

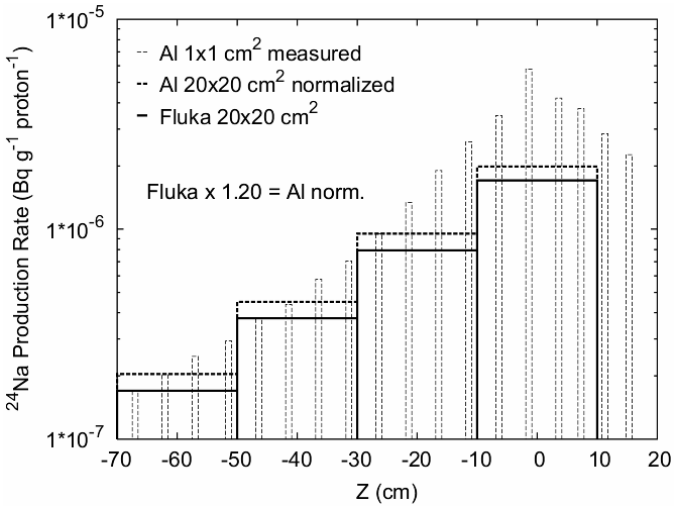

Figure 8: ^{24}Na Production rate at different distances from the beam axis predicted on 20x20 cm^2 Al foils from Montecarlo simulation (continuous line) compared with the one directly measured with the Activation-foils technique (dotted lines).

Silicon detectors were directly exposed in the IRRAD2 neutron field at ambient temperature without biasing them. After irradiation the devices were annealed for 4 min at 80 ºC and the leakage current at full depletion was measured. The leakage current value was converted to 1-MeV equivalent fluence (Φ_{eq}) following the NIEL scaling in Silicon [xxiii]. This method was chosen since it was previously demonstrated that the leakage current of fully depleted reverse biased silicon detectors does neither depend on the initial resistivity and conduction type nor on the oxygen and carbon content of the material [xxii]. They are thus offering a high reproducibility for fluence measurements even if different batches of detectors are used.

The results of this technique to calculate Φ_{eq} are shown in Fig. 9. The values obtained by the Silicon particle detectors used as Non-Ionizing Energy Losses (NIEL) proportional damage counters are here plotted versus the same quantity calculated from Monte Carlo simulations.

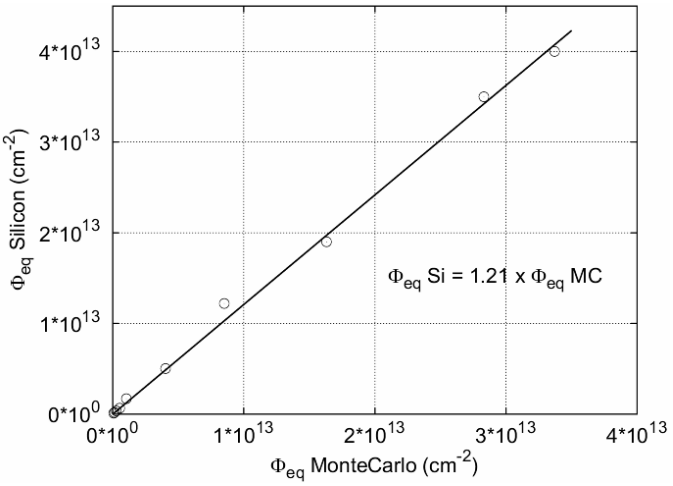

Figure 9: Equivalent fluence from Silicon detectors, plotted versus the equivalent fluence calculated from Monte Carlo simulations.

With respect to the Monte Carlo simulations the Φ_{eq} as measured by the silicon detectors shows a good linearity but is also overestimated by 21 %. The reason for these small differences between measurements and the simulation might be manifold. There was a practical difficulty to measure the activity of the short-lifetime ^{24}Na nuclide after each irradiation step allowed only for a few activation measurements. Furthermore, although great care was taken to have stable beam conditions during the one week running of the experiment, small variations can not be excluded. And finally the simulation itself and the NIEL scaling of the Silicon detector response might also be afflicted by a small error. Nevertheless, Silicon detectors were identified as a good tool for measuring Φ_{eq} and were thus used to plot the experimental data shown hereafter in Fig. 10.

Fig. 10 shows the comparison between the Total Ionization Dose (TID) in Aluminum estimated by simulations (empty round markers) and the values measured with the various dosimeter types (other markers in the plot). The TID deposed by the neutron/gamma environment in a thin Aluminum foils is supposed to be equal to the one expected in thin solid-state semiconductors devices.

The measurement performed with sensitive films, and PAD dosimeters are in average greater by a factor of 7.3 ± 2.7 % than the value predicted from simulations. The RPL technique shows instead a factor 3.2 ± 8.5 % greater than simulations. This difference is expected and is due to the different neutron interactions in the various sensitive materials constituting the employed dosimeters [xxiv]. In the IRRAD2 facility the neutron spectrum is dominated by fast and high-energy neutrons (85 % of the neutrons have energies from 10 keV to 1 MeV). In this range, neutrons deposit a significant fraction of their energy in Non-Ionizing Energy Losses (NIEL) and in inelastic interactions that produce fast-light particles that escape from semiconductor materials. The neutron contribution to the TID in semiconductors with respect to the gamma rays it is thus in the order of a few tens percent and results in a TID estimation smaller than the one obtained by other systems. This fact has been also proved in measuring doses in IRRAD2 by means of solid-state Silicon dosimeters [xxv].

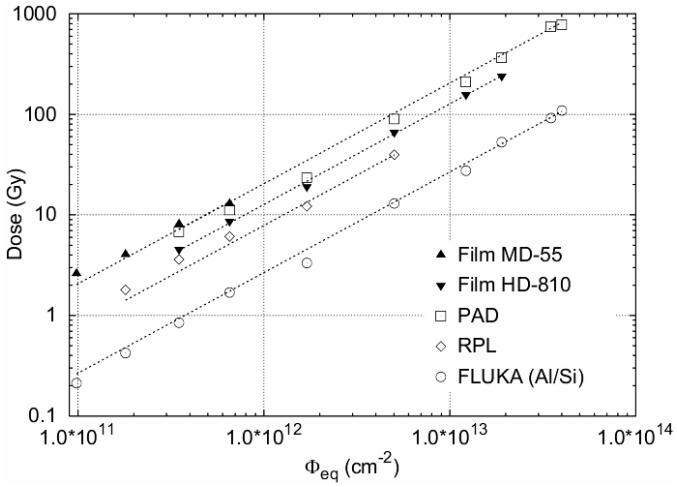

Figure 10: Comparison among the different TID measured at 50 cm from the beam axis obtained by different dosimetric means. The dotted lines have been plotted as guidelines within different data sets.

The most important mechanism responsible for transfer of energy from neutrons to polymeric

substances like PAD and Gafchromic films is instead elastic scattering. The recoil proton generated in this way will move through the material depositing the initial neutron energy via ionization leading to the increased response.

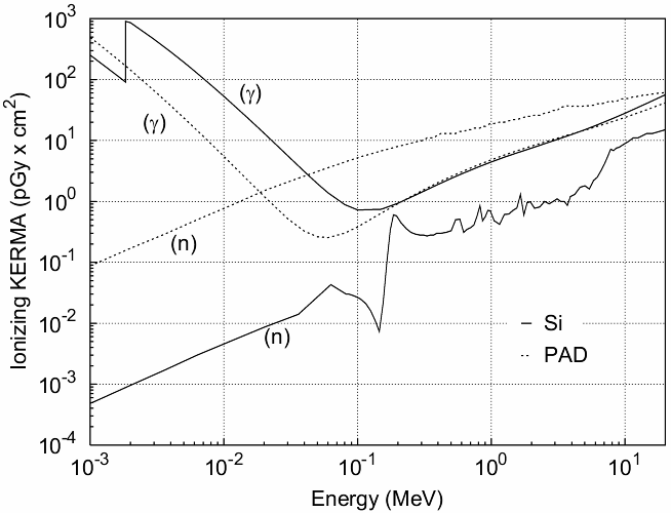

Figure 11: Neutron (n) and Photons (□) KERMA values in Si and PAD in the energy range 1-keV ÷ 20 MeV.

The Films and PAD measurement are therefore in good agreement and lie in an interval of ± 15 %. It has to be noted that the film MD-55 provides almost the same measurement of the PAD with an error of about ± 5 %.

The RPL response is a factor 2 lower with respect to the PAD in the IRRAD2 environment and lies thus in between the Alanine measurements and the simulation results. This discrepancy, already observed in a previous work [xxi], may be explained with an intermediate neutron interaction mechanism in the different material of the RPL (silver-activated aluminophosphate glass).

For the PAD dosimeters only, the above experimental data were compared to the theoretical calculation of the scaling factors for the TID released in PAD and Silicon that is the base material for solid-state dosimeters.

Fig. 11 shows the neutron and photon Ionizing KERMA values simulated for Silicon and PAD calculated from Ref. [[xxvi]] and [[xxvii]]. Folding these coefficients with the neutron and gamma spectra simulated for the IRRAD2 facility of Fig. 7, it is possible to calculate the absorbed dose expressed in Gy normalized to one incident proton. The results of these calculations are reported in Table 1.

Table I
ABSORBED DOSES CALCULATED FROM THE PARTICLE SPECTRA

	Silicon Gy/proton	PAD Gy/proton
Gammas	$D_{Si,} = 6.04 \times 10^{-15}$	$D_{PAD,} = 6.10 \times 10^{-15}$
Neutrons	$D_{Si,n} = 2{,}74 \times 10^{-15}$	$D_{PAD,n} = 1{,}52 \times 10^{-13}$

The ratio between the dose as measured in PAD and the dose deposed in Silicon as calculated by Monte Carlo is thus given by the following equation:

$$\frac{D_{PAD,IRRAD2}(reading)}{D_{Si,IRRAD2}(calculated)} = \frac{D_{PAD,\gamma} + k \times D_{PAD,n}}{D_{Si,\gamma} + D_{Si,n}} \qquad (2)$$

where the doses D are the ones reported in Table 1, and the coefficient k is the relative sensitivity of Alanine for neutrons compared to gamma rays [xxviii].

The relative response in Alanine to monoenergetic neutrons ranges from 0.36 to 0.7 compared with the response to ^{60}Co photons in the energy range from 0.5 to 15 MeV [xxix]. On the basis of the neutron spectrum of Fig. 7 a coefficient $k = 0.4$ has been found for the IRRAD2 facility.

By substituting all above data in Equation 2, the dose ratio PAD vs. Silicon in IRRAD2 turns out to be equal to 7.6. This is in good agreement with the experimental measurement presented in Fig. 10 which gave a factor of 7.3.

5. IRRADIATED SAMPLES HANDLING

Neutron and proton irradiations induce activation in the exposed materials. Equivalent dose-rates of hundreds of Sv/h can be reached at 10 cm distance from the samples and are essentially due to medium-life (years time scale) gamma and beta emitters generated by nuclear reactions in the materials themselves. Even if the remote controlled systems of the facilities minimize the radiation exposure during samples positioning, the storage and the post-exposure handling have to be well controlled and impose to follow the CERN radiation safety rules. These rules are continuously updated by the CERN Safety Commission [xxx] following the recommendation of the CERN member states in matter of protection against ionizing radiations.

During the samples cool-down period the Irradiation facilities disposed of several storage facilities at room and low temperature (e.g. -30 ºC), equipped to manipulate samples under safe conditions.

After appropriate cool-down (that depends on both irradiation level and specimen material composition), samples belonging to outside institutes can leave CERN following a new shipping procedure according to the Radiation Protection Procedure n. 13 (RPR-13) of January 2004. Details about these new rules can be found in Ref. [xxx] and [xxxi].

ACKNOWLEDGMENT

The authors wish to thank Dr. L. Dusseau from Montpellier University, France and Dr. D.F. Lewis, from ISP Advanced Materials Groups Wayne, NJ 07470, USA for providing the OSL and the Gafchromic films respectively used for beam profiling. We would like to express our tanks also to M. Huhtinen from CERN for the Monte Carlo simulations and the useful discussion about particle interaction in Silicon. Finally we wish also to tanks all the operators of the CERN-PS machine, especially R. Steerenberg.

REFERENCES

[1] The Large Hadron Collider Project Webpage [Online]. Available: http://www.cern.ch/lhc-new-homepage/.

[2] A. G. Holmes-Siedle, L. Adams, *Handbook of Radiation Effects* (second edition), Oxford University Press, 2002.

[3] M. Glaser, L. Durieu, F. Lemeilleur, M. Tavlet, C. Leroy, P. Roy, "New Irradiation zones at the CERN-PS", *Nucl. Inst. and Meth.*, A426, pp. 72-77, 1999.

[4] M. Glaser, F. Lemeilleur, M. Tavlet, "Radiation Test Facilities in the New PS East Hall at CERN", *IEEE Trans. Nucl. Sci.,* vol. 44, pp. 136 –141, 2000.

[5] L. Fernandez-Hernando, Ch. Ilgner, A. Macpherson, A. Oh, H. Pernegger, T. Pritchard, R. Stone, "A Beam Condition Monitor for the experimental areas of the LHC", presented at the 9th European Particle Accelerator Conference (EPAC 2004), Lucerne, Switzerland, 5-9 July 2004.

[6] K.E. Armsa, K.K. Gana, P. Jacksona, M. Johnsona, H. Kagana, R. Kassa, A.M. Rahimia, C. Rusha, S. Smitha, R. Ter-Antoniana, M.M. Zoellera, P. Buchholzb, M. Holderb, A. Roggenbuckb, P. Schadeb, M. Ziolkowski, "ATLAS pixel opto-electronics", *Nucl. Inst. and Meth.*, to be published, 2005.

[7] CERN-PH Department Irradiation Facilities Webpage [Online]. Available: http://cern.ch/irradiation/.

[8] LHC Experiment Radiation Monitoring Working Group, RADMON [Online]. Available: http://www.cern.ch/lhc-expt-radmon/.

[9] K. Bernier, G. de Rijk, G. Ferioli, E. Hatziangeli, A. Marchionni, V. Palladino, G.R. Stevenson, T. Tabarelli and E. Tsesmelis, "Calibration of Secondary Emission Monitors of Absolute Proton Beam Intensity in the CERN SPS North Area", *CERN Yellow Report 97-07*, 1997

[10] A. Fassò, A. Ferrari, J. Ranft, P.R. Sala, "FLUKA: Status and Prospective for Hadronic Applications", in Proc. of the MonteCarlo 2000 Conference, Lisbon, October 23-26, 2000, Springer-Verlag Berlin, pp. 955-960, 2001.

[11] E. Leon-Florian, C. Leroy and C. Furetta, "Particle Fluence Measurements by Activation Technique for Radiation Damage Studies", CERN Divisional Report, *CERN-ECP-95-15*, 1995

[12] A.H. Sullivan, *A Guide to Radiation and Radioactivity Levels Near High-energy Particle Accelerators*, Nuclear Technology Publishing, London, UK, 1992.

[13] Gafchromic® Radiochromic Dosimetric Films Datasheets [Online]. Available: http://www.ispcorp.com.

[14] L. Dusseau, G. Polge, S. Matias, J.R. Vaillé, R. Germanicus R. Broadhead, B. Camanzi, M.Glaser, F. Saigne, J. Fesquet, J. Gasiot, "High-energy particle irradiation of optically stimulated luminescent films at CERN", *IEEE Trans. Nucl. Sci.,* vol. 48, pp. 2056–2066, 2001.

[15] N. V. Klassen et al, "Gafchromic MD-55: Investigated as a precision dosimeter", *Med. Phys.,* vol. 24(12), pp. 1924-1934.1997

[16] O. Missous, F. Loup, J. Fesquet, H. Prevost, J. Gasiot, "Optically Stimulated Luminescence of Rare-earth Doped Phosphors", *Eur. J. Solid State Inorg. Chem.,* vol. 28/s, pp. 163,166, 1991.

[17] D. Plattard, G. Ranchoux, L. Dusseau, G. Polge, J-R. Vaillé, J. Gasiot, J. Fesquet, R. Ecoffet, N. Iborra-Brassart, "Characterization of an Integrated Sensor Using Optically Stimulate Luminescence for In-flight Dosimetry", *IEEE Trans. Nucl. Sci.,* vol. 49, pp. 1322 –1326, 2002.

[18] G. Polge, L. Dusseau, S. Matias, D. Gensanne, D. Plattard, J. Fesquet, J. Gasiot, et al. "Applications to radiotherapy of a dose-mapping system based on the optically stimulated luminescence", *in Proc. IEEE Medical Imaging Conf.,* Lyon, France, Oct. 2-6, 2000.

[19] V. Pugatch, K.T. Knopfle, Yu. Vassiliyev, "Beam Profile Imaging Target", *Nucl. Phys. A 701*, pp. 204c-208c, 2002.

[20] H. Vincke, I. Brunner, M. Huhtinen, "Production of radioactive isotopes in Al, Fe, Cu-samples by stray radiation fields at proton accelerator", CERN, CERN-TIS-2002-007-RP, 2002.

[21] F. Coninckx, H. Schonbacher, M. Tavlet, G. Paic, D. Razem, "Comparison of high-dose dosimetry systems for radiation damage studies in collider detectors and accelerators", *Nucl. Inst. and Meth.,* vol. B83, pp. 181-188, 1993.

[22] M. Moll, E. Fretwurst, G. Lindström, "Leakage current of hadron irradiated silicon detectors – material dependence", *Nucl. Inst. and Meth,* vol. A426, pp. 87-93, 1999.

[23] M. Moll, E. Fretwurst, M. Kuhnke, G. Lindström,"Relation between microscopic defects and macroscopic changes in silicon detector properties after hadron irradiation", Nucl. *Inst. and Meth,* vol. B186, pp. 100-110, 2002.

[24] M.H. Van de Voorde, "Effects of radiation on materials and components – Megarad dosimetry", CERN, Yellow Report 69-12, 1969.

[25] F. Ravotti, M. Glaser, M. Moll, K. Idri, J-R. Vaillé, H. Prevost, and L. Dusseau, "Conception of an Integrated Sensor for the Radiation Monitoring of the CMS Experiment at the Large Hadron Collider", *IEEE Trans. Nucl. Sci,* vol. 51 (6), pp. 3642-3648, 2004.

[26] M. B. Chadwick, H H, Barschall et al., "A consistent set of neutron kerma coefficients from thermal to 150 MeV for biologically important materials", *Med. Phys.*, vol. 26, pp. 974-991, 1999.

[27] J. H. Hubbell, "Photon mass attenuation and energy absorption coefficients from 1 keV to 20 MeV", *Int. J. Appl. Radiat. Isot.,* vol. 33, pp. 1269-1290, 1982.

[28] Y. Katsumura, Y. Tabata, T. Seguchi, N. Morishita, T. Kojima, "Fast neutron irradiation effects – III. Sensitivity of alanine systems for fast neutron having an energy of ~ 1 MeV", *Radiat. Phys. Chem.,* vol. 28 (4), pp. 337-341, 1986.

[29] H. Schraube, E. Weitzenegger, A. Wieser, D. F. Regulla, "Fast neutron response of alanine probes", *Appl. Radiat. Isot.,* vol. 40, pp. 941-944, 1989.

[30] Documents of the CERN Safety Commission-Radiation Protection (RP) group [Online]. Available: http://cern.ch/radiation-protection/.

[31] CERN SC-RP Radioactive Shipping Informations [Online]. Available: http://cern.ch/rp-shipping.